Proceedings of the ASME 2010 3rd Joint US-European Fluids Engineering Summer Meeting and 8th International Conference on Nanochannels, Microchannels, and Minichannels
FEDSM-ICNMM2010
August 1-5, 2010, Montreal, Canada

FEDSM-ICNMM2010-31253

CHARACTERIZATION OF LOW REYNOLDS NUMBER WIND TURBINE AERODYNAMICS BY BEM THEORY AND PIV MEASUREMENTS

A. Villegas Vaquero
Rutgers, The State University of New Jersey
Piscataway, NJ, USA

Y. Cheng
Rutgers, The State University of New Jersey
Piscataway, NJ, USA

V. del Campo
ETSEIAT, UPC
Terrassa, Spain

F. J. Díez
Rutgers, The State University of New Jersey
Piscataway, NJ, USA

ABSTRACT

In this study, low Reynolds number wind turbine aerodynamics was considered. The overall goal was to characterize the flow in order to optimize the power output of the system. First, BEMT theory (Blade Element Momentum Theory) was formulated for this flow where Prandtl's tip- and hub-loss corrections were included, as well as Glauert's thrust coefficient correction. The theory was validated with experimental data from National Renewable Energy Laboratory (NREL) for larger scale wind turbines. Also, a physical model of a low Reynolds number horizontal-axis wind turbine (HAWT) was built. Particle Image Velocimetry (PIV) was used to calculate the velocity field around the HAWT. This allowed for planar measurements of the velocity field at different location in the wake of the rotor. The measurements were performed in a water channel allowing for better control of PIV seeding and improved flow visualization. PIV results allowed observation of the velocity field and vorticity field in the wake of the rotor. This data is currently being compared to BEMT theory suggesting good agreement.

INTRODUCTION

Aerodynamics and wake structure of wind turbines have been widely studied for power optimization and noise reduction. Usually, mid to high Reynolds number wind turbines are the object of study, with almost no work focusing on very Low Reynolds number, were very few data is available. Low Reynolds numbers can be found in water channel experiments with wind turbine models.

Blade element momentum theory (BEMT) is still widely used for estimations of the aerodynamics of wind turbines (Burton et al. 2001; Hansen 2008). As BEMT is based on some invalid assumptions, it is corrected by introducing empirical adjustments (Prandtl and Betz 1927; Glauert 1935). BEMT is used to calculate aerodynamic properties in the plane of the rotor for high Reynolds numbers.

The development of numerical simulations is necessary for a better understanding of the fluid around the wind turbine. The purpose of the simulations is to get the velocity and vorticity field and see if they agree with experiments to validate the code. A good review in wind turbine wake structures can be found in Vermeer, Sorensen, and Crespo 2003. Some research studies about vortex structure have compared experimental particle image velocimetry (PIV) results and numerical simulations (Whale et al. 2000; Grant et al. 2000). Whale's work shows experimental data taken by PIV measurements in a water channel. Results showed that near wake structure of a model wind turbine in a water channel shares some of the fundamental characteristics of that of a full-scale unit, whose similarity is evident in the vorticity maps (Medici and Alfredsson 2006).

On full scales, wind turbines run at high Reynolds numbers. National Renewable Energy Laboratory (NREL) has played an important role in testing large scale wind turbines for the National Aeronautics and Space Administration (NASA) installations. Their investigations are based on their own wind turbines with their own airfoils. They have run numerous tests acquiring a large experimental database (Giguere and Selig 1999) and also validating the new models that they build. Other authors obtained experimental data and data visualization through diverse techniques such as PIV (Grant and Parkin 2000; Hirahara et al. 2005; Massouh and Dobrev 2007; Hossain et al. 2007), smoke-visualization (Haans et al. 2005), and hot-wire anemometry (Medici and Alfredsson 2006).

The purpose of this project is to test a new design of wind turbine by applying PIV technique in a water channel. First, a code based on BEMT was developed mainly to obtain the velocity field in the rotor plane but also to obtain other aerodynamic characteristics for Horizontal Axis Wind Turbines (HAWT's) that will be discussed below. The BEMT theory was improved by using Prandtl's tip- and hub-loss corrections and Glauert's correction. Results from the code were compared with experimental data from the National Renewable Energy Laboratory (NREL) to validate such code. Second, after validating the code, simulations for low Reynolds HAWT's were run. A new wind turbine model was created by optimizing the power output using the code for a very low Reynolds number. This a main difference with one of BEMT assumptions (high Reynolds number). The model was tested in a water channel, obtaining the experimental data and data visualization form PIV measurements in the vicinities of the rotor. Using a water channel instead of a wind tunnel removes dispersion and concentration seeding problems. Finally, conclusions and future work about the present work are given in the last section.

NOMENCLATURE

a	Axial Induction Factor
a'	Tangential Induction Factor
B	Number of Blades
BEMT	Blade Element Momentum Theory
BET	Blade Element Theory
c	Chord
C_d	Drag Coefficient
C_l	Lift Coefficient
c_t	Tip Chord
D	Drag
f	Prandtl's Tip- and Hub-Loss Correction
f_H	Prandtl's Hub-Loss Correction
f_T	Prandtl's Tip-Loss Correction
F_T	Tangential Force
HAWT	Horizontal Axis Wind Turbine
L	Lift
MT	Momentum Theory
NREL	National Renewable Energy Laboratory
P	Power
Q	Torque
r	Blade Radial Distance
R	Rotor Radius
T	Thrust
U	Axial Velocity
U_∞	Upstream Wind Velocity
V	Tangential Velocity
W	Relative Velocity
x	Blade Station
x_R	First S809 Airfoil Station

.

Greek symbols

α	Angle Of Attack
β	Twist Angle
λ	Tip Speed Ratio
λ_r	Local Tip Speed Ratio
ρ	Fluid Density
σ	Blade's Solidity
σ_r	Local Blade's Solidity
φ	Inflow Angle
Ω	Rotor's Rotational Speed
θ	Local Pitch Angle
θ_P	Pitch Angle

1. Blade Element Momentum Theory

Blade element momentum theory is the most commonly used method for calculating induced velocities on wind turbine blades. It is composed of two theories, Momentum Theory (MT) and Blade Element Theory (BET). The flow is supposed to be uniform, wind speed constant over rotor plane and no yawed flow, windshear or tower shadow are not taking in consideration.

1.1 Momentum Theory

Momentum theory is based on the following hypotheses: uni-dimensional flow, quasi-steady; incompressible; no viscous effects; and no external forces acting in the flow upstream and downstream of the rotor. This theory assumes that loss of pressure or momentum in the rotor plane is caused by the work done by the airflow passing through the rotor plane. Using MT, it is possible to calculate induced velocities on the blade, from the momentum lost in the flow, in the axial and tangential directions.

The way to relate the axial wind speed at the rotor plane, U_{RP}, with the free upstream wind speed, U_∞, is the axial induction factor, a, as:

$$U_{RP} = (1 - a)\,U_\infty \tag{1}$$

Momentum theory also considers that the rotor disc is composed of a multiplicity of blades.

Momentum theory also introduces the effect of the rotation of the wake. This effect is presented by the tangential induction factor, a'. That parameter relates the tangential wind speed at the rotor plane, V_{RP}, with the rotor's speed rotation, Ωr, as:

$$V_{RP} = (1 + a')\,\Omega\, r \tag{2}$$

where, Ω is the rotor's angular speed and r is the radial distance from the center of the rotor along the blade span.

Distributions of thrust, dT_{MT}, torque, dQ_{MT}, and power, dP_{MT}, along the blade span are obtained when applying MT to a HAWT. Equations are given by:

$$dT_{MT} = 4\pi\rho U_{\infty}^{2} a(1-a) r dr \quad (3)$$

$$dQ_{MT} = 4\pi\rho U_{\infty}(1-a)\Omega a' r^{3} dr \quad (4)$$

$$dP_{MT} = \Omega \, dQ_{MT} \quad (5)$$

where, ρ is the density of the fluid in which the rotor is immersed-

1.2 Blade Element Theory

The other part of BEMT, blade element theory, assumes that each radial element acts independent of surrounding elements and operates as 2-D airfoils. In addition, it ignores the velocity component in the span wise direction.

In BET theory it is possible to observe the angles, velocities and forces acting in each blade element. Every blade element sweeps out an angular ring with each rotation. The same induction parameters revealed in MT are introduced in this theory (*a* and *a'*).

The relative velocity, *W*, seen by a section of the blade is a combination of the axial velocity, *U*, and the tangential velocity, *V*, and it is expressed by:

$$W = \sqrt{U_{\infty}^{2}(1-a)^{2} + \Omega^{2} r^{2}(1+a')^{2}} \quad (6)$$

where everything is known from MT.

Also, the lift, L, and the drag, D, per length unit are perpendicular and aligned, respectively, to the relative velocity for each element of the blade. Then, thrust, *T*, and tangential force, F_T, per length unit can be obtained projecting lift and drag in the normal and tangential direction, respectively, as:

$$T = L\sin(\phi) + D\cos(\phi) \quad (7)$$

$$F_T = L\cos(\phi) - D\sin(\phi) \quad (8)$$

where, φ is the inflow angle, that is, the angle between the relative velocity, *W*, and the plane of rotation. Inflow angle is composed by the local pitch angle, θ, and the angle of attack, α, as:

$$\phi = \theta + \alpha \quad (9)$$

Local pitch angle is the angle between the chord, *c*, and the plane of rotation. This angle can be written as a combination of the pitch angle, θ_p, and the twist distribution along the blade, β, as:

$$\theta = \theta_P + \beta \quad (10)$$

where θ_p is used to be referred as the angle between the tip chord, c_t, and the plane of rotation and β is used to be measured relative to the tip chord.

Applying BET to a HAWT, distributions of thrust, dT_{BET}, tangential force, dF_{TBET}, torque, dQ_{BET}, and power, dP_{BET}, along the radial blade axis are obtained. Each equation is multiplied by the number of blades, *B*, of the rotor and they are given by:

$$dT_{BET} = \frac{1}{2}\rho W^{2} cB\left[C_l\cos\phi + C_d\sin\phi\right]dr \quad (11)$$

$$dF_{t_{BET}} = \frac{1}{2}\rho W^{2} cB\left[C_l\sin\phi - C_d\cos\phi\right]dr \quad (12)$$

$$dQ_{BET} = \frac{1}{2}\rho W^{2} cB\left[C_l\sin\phi - C_d\cos\phi\right]r dr \quad (13)$$

$$dP_{BET} = \frac{1}{2}\rho W^{2} cB\left[C_l\sin\phi - C_d\cos\phi\right]\Omega r dr \quad (14)$$

with,

$$C_l = \frac{L}{\frac{1}{2}\rho W^{2} c} \quad (15)$$

$$C_d = \frac{D}{\frac{1}{2}\rho W^{2} c} \quad (16)$$

where, C_l is the lift coefficient and C_d is the drag coefficient for each blade station.

1.3 BEMT

Coupling those two theories results in the BEMT. By equating the thrust and torque from both theories, the two equations needed to solve the problem can be obtained. The next equations can be found in Burton et al. 2001 and show that

$$\begin{cases} dT_{MT} = dT_{BET} \\ dQ_{MT} = dQ_{BET} \end{cases} \quad \begin{cases} \dfrac{a}{1-a} = \dfrac{\sigma_r}{4}\left[\dfrac{C_l\cos\phi + C_d\sin\phi}{\sin^{2}\phi}\right] & (17) \\ \dfrac{a'}{1+a'} = \dfrac{\sigma_r}{4}\left[\dfrac{C_l\sin\phi - C_d\cos\phi}{\sin\phi\cos\phi}\right] & (18) \end{cases}$$

with,

$$\sigma_r = \frac{Bc}{2\pi x R} = \frac{\sigma}{x} \quad (19)$$

$$\tan\phi = \frac{1}{\lambda_r}\left(\frac{1-a}{1+a'}\right) \quad (20)$$

$$\lambda_r = \frac{\Omega r}{U_{\infty}} = \lambda x \quad (21)$$

where,

σ	=	Solidity of the blade
σ_r	=	Local solidity of the blade
R	=	Rotor's radius
x	=	Dimensionless radial blade station, *r/R*
λ	=	Tip speed ratio
λ_r	=	Local tip speed ratio

Equations (18) and (17) will be solved to obtain the axial induction factor, *a*, and the tangential induction factor, *a'*, following an iterative process. Then, these values will be used to determine velocities and aerodynamic forces in the rotor plane.

Corrections made by Prandtl (Prandtl and Betz 1927) for the tip- and hub-loss (f_T and f_H), are given respectively by:

$$f_T(x) = \frac{2}{\pi} arc\cos\left[exp\left(-\frac{B}{2}\frac{1-x}{x}\frac{1}{sen(\phi)} \right) \right] \quad (22)$$

$$f_H(x) = \frac{2}{\pi} arc\cos\left[exp\left(-\frac{B}{2}\frac{x-x_R}{x}\frac{1}{sen(\phi)} \right) \right] \quad (23)$$

where, x_R is the first radial airfoil station from the center of the hub, that is, where the transition from the hub finish and the aerodynamic airfoil start.

The global Prandtl's correction function is then given by:

$$f(x) = f_T(x) \cdot f_H(x) \quad (24)$$

Introducing this correction into BEMT, equations (18) and (17) become:

$$\frac{a}{1-a} = \frac{\sigma_r}{4f}\left[\frac{c_l \cos\phi + c_d \sin\phi}{\sin^2\phi} \right] \quad (25)$$

$$\frac{a'}{1+a'} = \frac{\sigma_r}{4f}\left[\frac{c_l \sin\phi - c_d \cos\phi}{\sin\phi\cos\phi} \right] \quad (26)$$

The same iteration process will be followed to obtain *a* and *a'* for those last two equations corrected by the Prandtl's factor.

Another correction was made by Glauert (Glauert 1935) over the classic theory. By comparing experimental data with BEMT, it was discovered that the thrust coefficient agreed well below a critical axial induction factor. Above this critical number, around 0.4, Cp did not agree. This happens because the rotor enters on what is known as the turbulent wake state. In that state, the flow comes from the outside of the wake and increases the turbulence in the far wake. Therefore, the flow after the rotor decreases its speed but the thrust keeps increasing. This correction can be applied to BEMT theory by obtaining a correlation from experimental data.

For example, when *a* is bigger than 0.4, equation 25 can be replaced by the correction

$$a = \frac{1}{2}\left[2 + K(1-2a_c) - \sqrt{\left(K(1-2a_c)+2\right)^2 + 4\left(Ka_c^2 - 1\right)} \right] \quad (27)$$

where,

$$K = \frac{4F\sin^2\phi}{\sigma C_n}$$

$$C_n = C_l\cos\phi - C_d\sin\phi$$

2. MATLAB Code Results

The discussed BEMT theory and the multiple corrections were coded in MATLAB for easy analysis of all the different variables. The user needs to input the geometry of the airfoil or used some proven geometries. The code was validated using the rotor geometry from one of the National Renewable Energy Laboratory wind turbine designs (Hand et al. 2001). Characteristics of the rotor are described in ANNEX A (Fig. 27 and Table 1.a). Some results from the code will be shown next.

Fig. 1 and Fig. 2 show the chord distribution, *c(x)*, and the local pitch angle distribution, φ(x), along the blade span respectively. Fig. 1 shows the lineal chord distribution along the blade span, decreasing from the root to the tip. The transition from the center of the rotor to the first airfoil station is not represented in the plot.

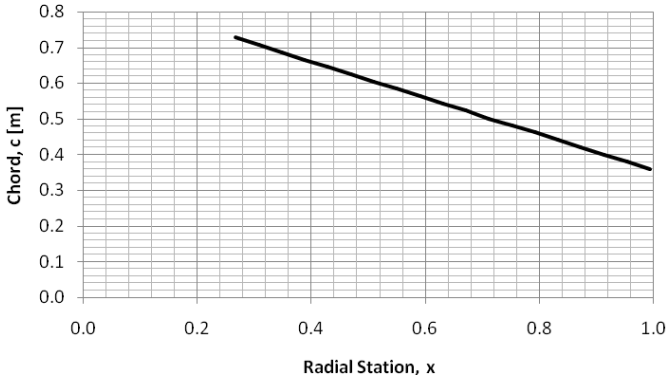

Fig. 1. Chord distribution along the blade span

Local pitch angle distribution is shown in Fig. 2 for a fixed pitch angle of 5 degrees. It is varying from the highest value in the root to the lowest value in the tip exponentially. The pitch angle is referred to the 75% of the blade span and not to the tip of the blade as usual. Thus, the local pitch angle would be 5 degrees in the 75 % of the blade span.

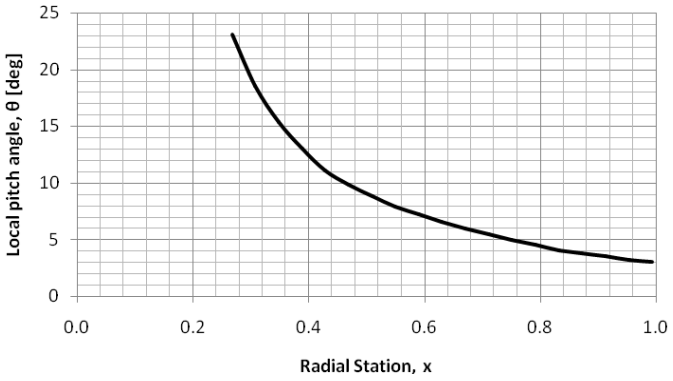

Fig. 2. Local pitch angle distribution along the blade span

Once the geometry is known, lift and drag coefficients should be included in the code as functions of the angle of attack to be able to solve equations. These tables could be obtained from different methods: (1) analytical methods; (2) use of computer programs that can obtain some of the main aerodynamic characteristics of the airfoil; and (3) experimental data.

In order to achieve the best accuracy possible the third method was selected, taking the coefficients from the experimental data from the NREL (Hand et al. 2001). The airfoil selected was the S809 airfoil. Table 2.a in ANNEX 2 shows this data for a Reynolds number of 1000000.

Fig. 3 and Fig. 4 show the experimental points taken from the NREL. A polynomial approximation curve was created for those experimental points in order to introduce lift and drag coefficients in the equations.

A sixth order polynomial approximation works well for fitting available data points. Both polynomial equations are shown in each plot (Fig. 3 and Fig. 4).

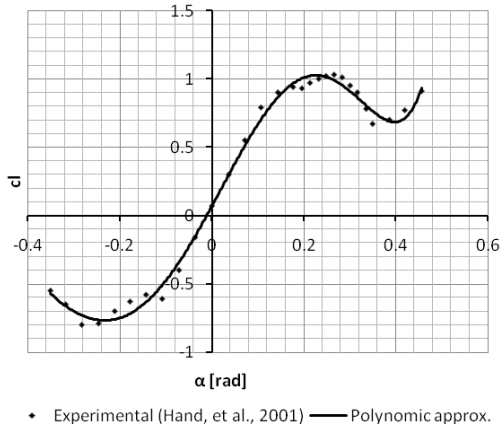

Fig. 3. Experimental lift coefficient vs angle of attack. Also shown is the fitting curve for those experimental points

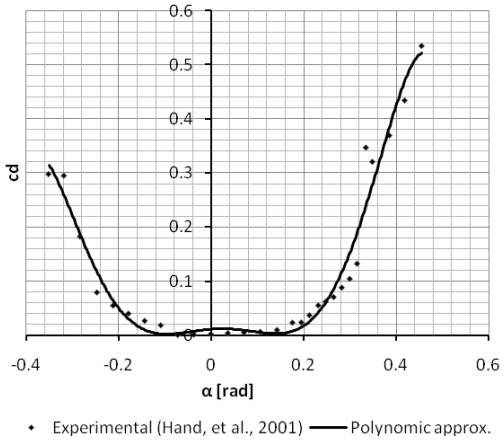

Fig. 4. Experimental drag coefficient vs the angle of attack. Also shown is the fitting curve for those experimental points

3. Results and comparison

Plots from Fig. 5 to Fig. 18 represent the aerodynamic characteristics along the blade for an upstream velocity of 9 m/s, rotor's rotational speed of 72 r.p.m., where the air density value used was 1.225 kg/m^3 and the Reynolds number was 1,000,000. The rotor is a two-bladed rotor with a diameter of 10.06 m. It is fixed at a pitch angle of 5 degrees.

Analytical values are compared with experimental values from NREL (Giguere and Selig 1999; Tangler 2002), for a virtual blade with the same airfoil and dimensions. In Fig. 5 to Fig. 18, the X axis is the non-dimensional radial station which is the radial distance from the center of the rotor along the blade span divided by the rotor diameter. The Y axis in each Fig. 5 to Fig. 18 contains the variation of the following parameters with *x*: (1)axial induction factor, *a;* (2) tangential induction factor, *a'*; (3) local pitch angle, φ; (4) angle of attack, α; (5) axial velocity, *U*; (6) tangential velocity, *V*; (7) total velocity, *W*; (8) circulation, γ; (9) lift coefficient, C_l; (10) drag coefficient, C_d; (11) Reynolds number, *Re*; (12) Normal force, *N*; (13) Tangential force, F_T; (14)Torque, Q.

From Fig. 5, Fig. 8 and Fig. 13 it is possible to observe a good qualitative and quantitative agreement between experiments and theory. Classic theory is not valid for the zone closer to the tip of the blade.

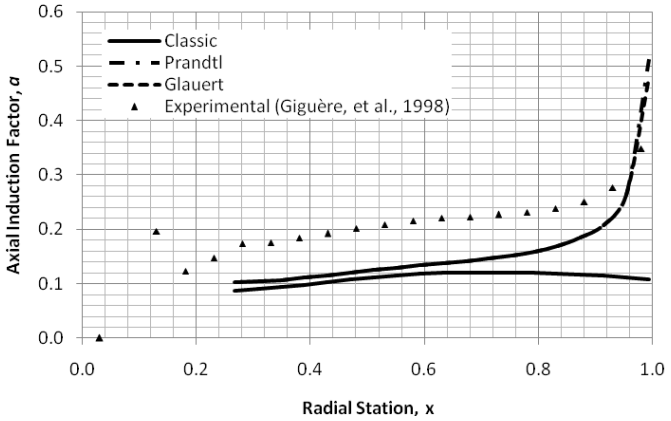

Fig. 5. Axial induction factor distribution along the blade span

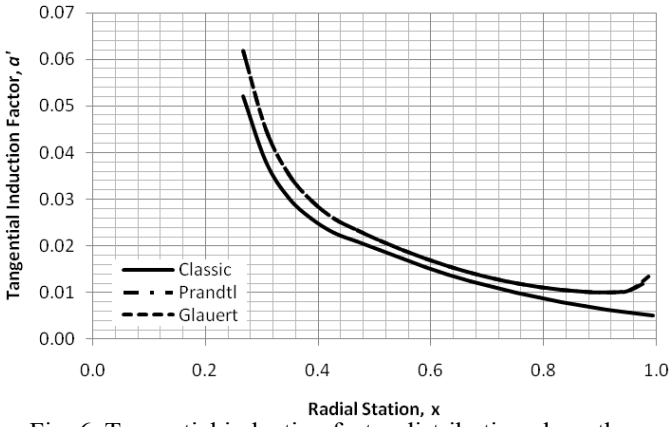

Fig. 6. Tangential induction factor distribution along the blade span

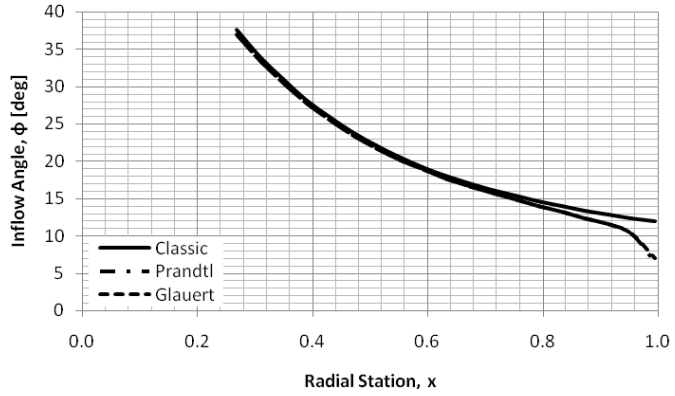

Fig. 7. Local pitch angle distribution along the blade span

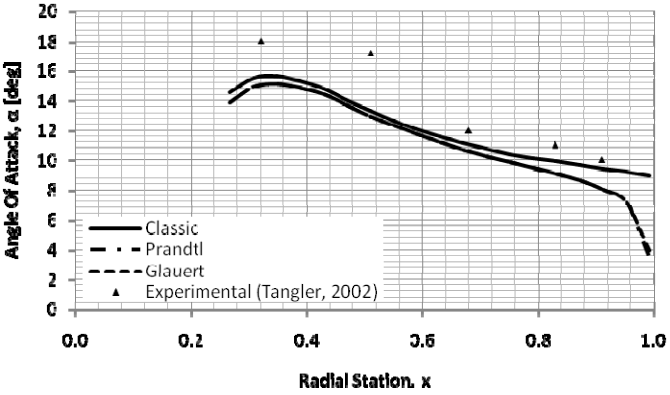

Fig. 8. Angle of attack distribution along the blade span

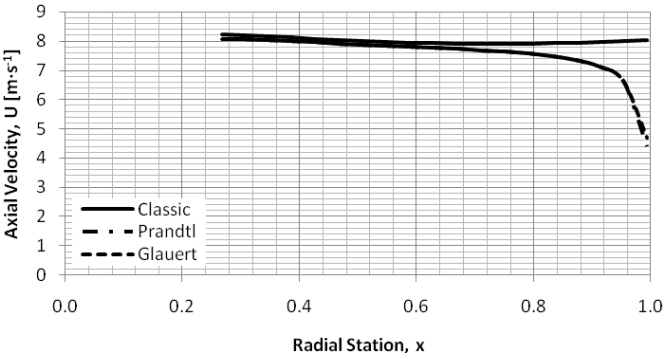

Fig. 9. Axial velocity distribution along the blade span

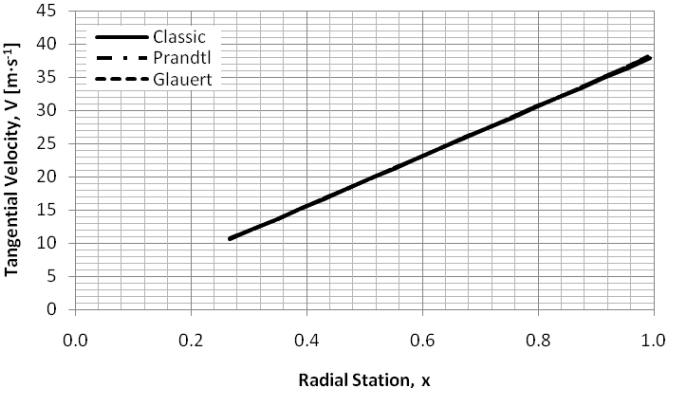

Fig. 10. Tangential velocity distribution along the blade span

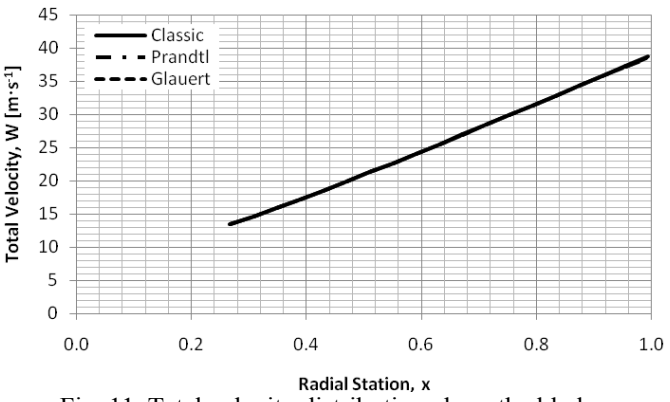

Fig. 11. Total velocity distribution along the blade span

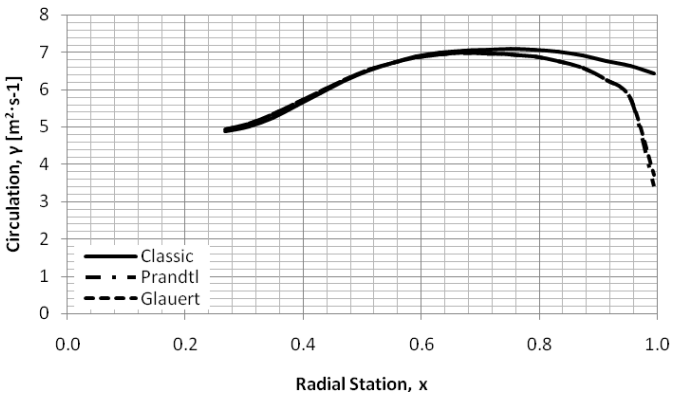

Fig. 12. Airfoil circulation distribution along the blade span

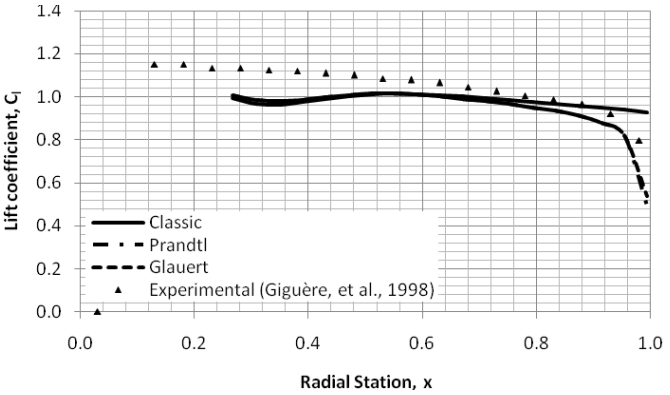

Fig. 13. Lift coefficient distribution along the blade span

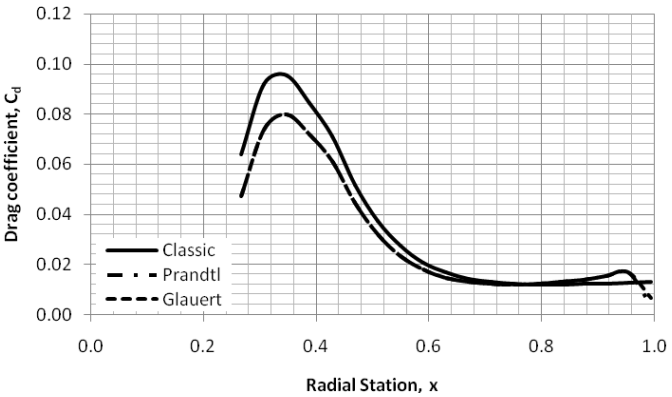

Fig. 14. Drag coefficient distribution along the blade span

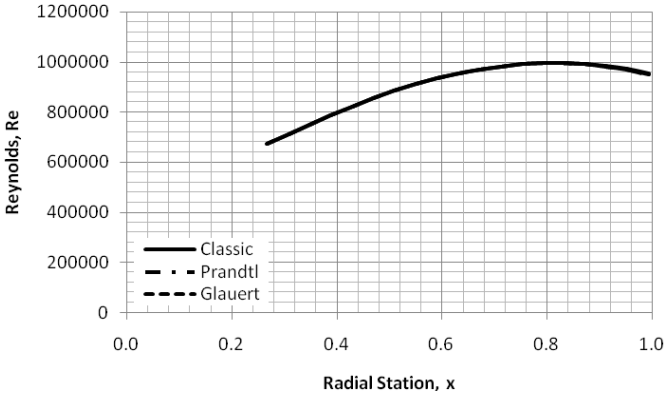

Fig. 15. Reynolds number distribution along the blade span

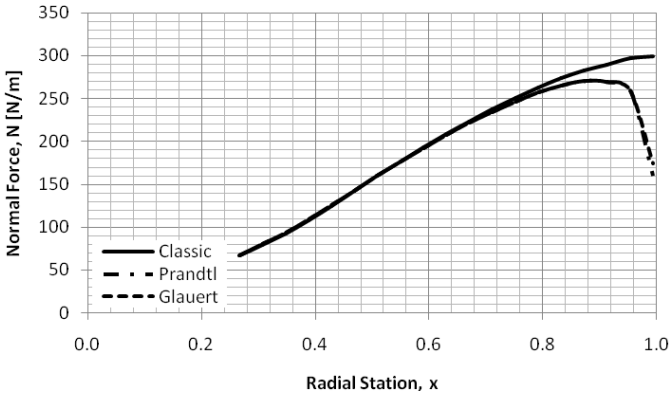

Fig. 16. Normal force distribution along the blade span

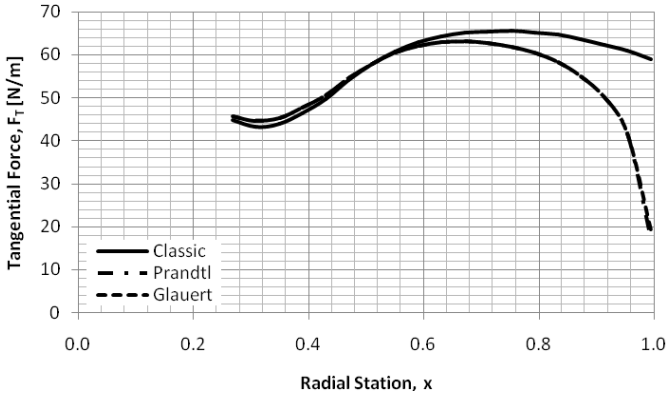

Fig. 17. Tangential force distribution along the blade span

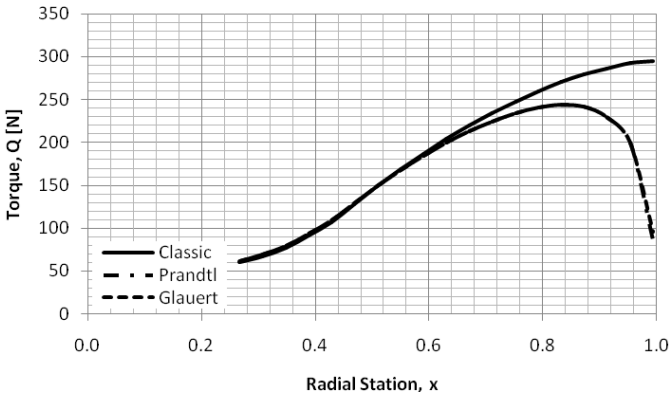

Fig. 18. Torque distribution along the blade span

Fig. 19 and Fig. 20 illustrate the power and thrust variation with the free upstream wind speed. The wind speed is varying from 5 m/s to 20 m/s. Good qualitative and quantitative agreement between experimental data and BEM theory is shown for wind speed lower than 12 m/s. After that value, the airfoils start getting stall and the performance of the wind turbine is more difficult to predict by the theory. Also, the polynomial approximation for C_l and C_d of the experimental data does not adequately represent the aerodynamic characteristics.

There are some formulas to predict the stall of the airfoil as Viterna and Corrigan 1982. This prediction for stall mode is used with BEM theory and compared with experimental results by some authors (Myers and Bahaj 2006; Tangler and Kocurek 2005).

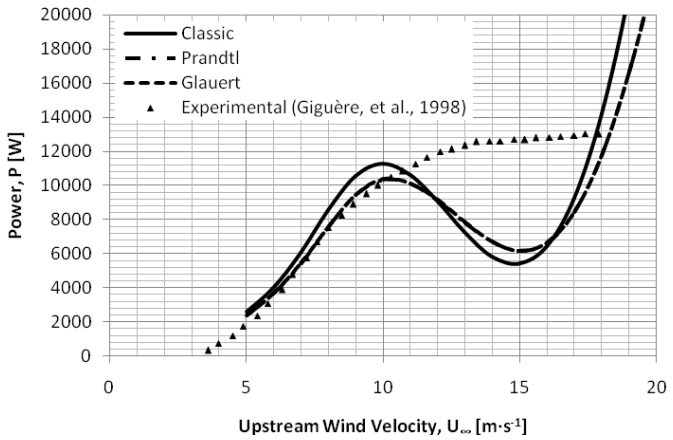

Fig. 19. Power variation with the free upstream wind speed

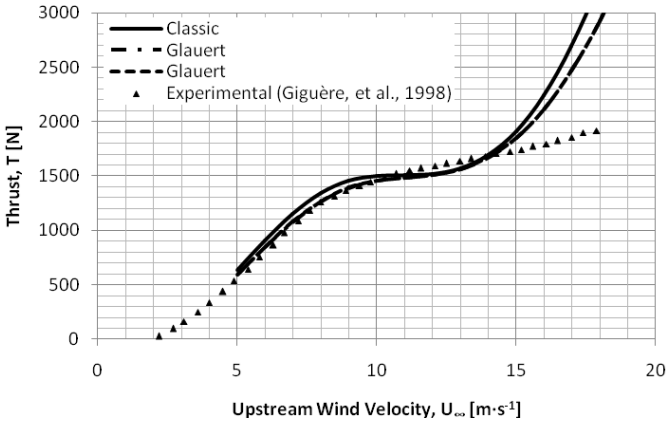

Fig. 20. Thrust variation with the free upstream wind speed

Fig. 21 exhibits the power coefficient variation with the tip speed ratio. As the rotor's speed rotation is constant, the tip speed ratio will vary inversely with the free wind speed. Again, a good agreement between experimental data and BEM theory can be perceived.

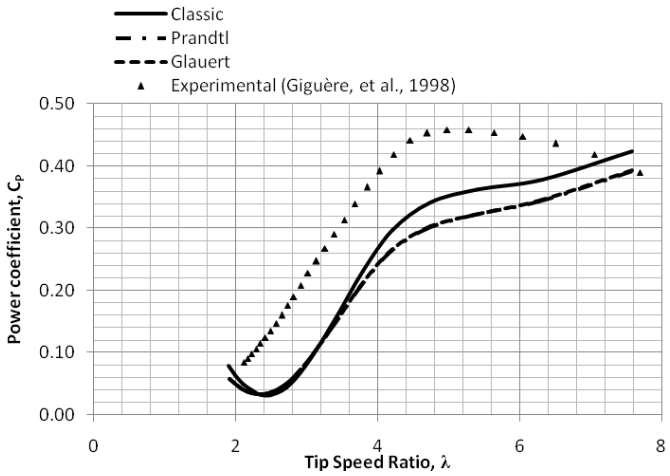

Fig. 21. Power coefficient variation with the tip speed ratio

4. Novel wind turbine design

After validating the code for high Reynolds number wind turbines, a new model was developed from several simulations for low Reynolds number. Characteristics of the blade geometry are shown in Table 1.b in ANNEX A. Also, Fig. 22 and Fig. 23 plot that data. Aerodynamic coefficients for the airfoil selected (GOE 531) are given in Table 2.b in ANNEX B.

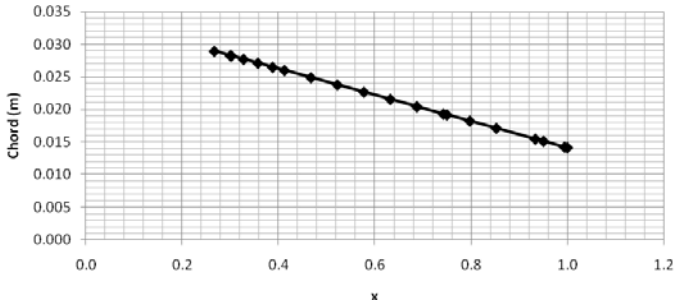

Fig. 22. Chord distribution along the blade span

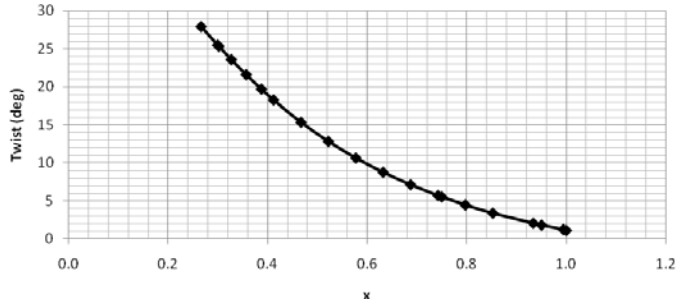

Fig. 23. Twist distribution along the blade span

5. Experimental Study of the Wake behind Wind Turbine

5.1 Experimental Setup

The experiments were conducted in a recirculating water tunnel located in the Department of Mechanical and Aerospace Engineering at Rutgers, the State University of New Jersey. Two sets of honeycombs and flow straighteners were placed upstream of the test section to ensure laminar flow conditions with turbulence levels below 0.1%. The dimension of the test section is 0.9 x 0.5 m2. The water free stream velocity was held constant at a value of 0.2m/s. The water was seeded with hollow glass spheres of 8-12 μm in diameter as tracer particles. The two-bladed wind turbine of 10 cm radius with various twists and chord lengths at different sections (Appendix A) was mounted on a low-friction bearing facing the flow direction. The flow drove the wind turbine to rotate at a constant speed of 47 rpm. The Reynolds number based on the diameter of the blades was 29,880.

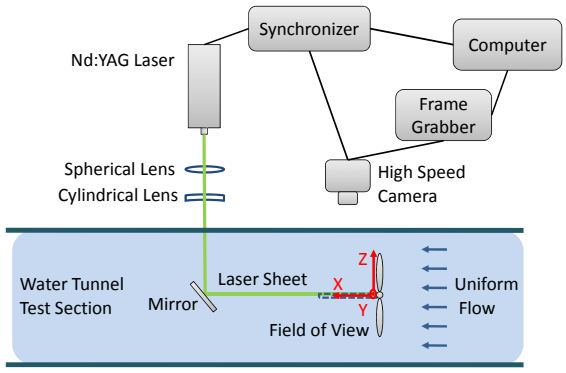

Fig. 24. Schematic diagram of experimental setup

A time-resolved PIV system was used to visualize the flow behind the wind turbine. A schematic diagram of the PIV system is shown in Fig. 24. The system consisted of a high frame rate dual-pulsed Nd:YAG laser of 10mJ/pulse at 1000Hz, a set of cylindrical and spherical lenses and mirrors to generate the laser sheet at the test section, a high speed Photron Ultima APX CMOS camera having the resolution of 1024 x 1024 pixels^2 at 2000 frames per second, a 1 ns resolution synchronization unit and a computer for data acquisition. The coordinate system is illustrated in Fig. 24. The flow moves along positive x direction.

5.2 Experimental Results

Fig. 25.a shows an instantaneous vector field and velocity contour of the near wake behind the wind turbine. The vectors represent the modified velocity of the wake by subtracting the free stream velocity and the contour color describes the subtracted in-plane velocity magnitude. As can be seen, the

flow field is immediately behind the turbine blade, and has a field of view of 1.3R x 1.3R. The blade generated a motion of circulation behind it, leaving a coupled high velocity and low velocity region, which can be represented by vorticity. An instantaneous vorticity contour plot is shown in Fig. 25.b. The vorticity was calculated using $\omega = \partial v/\partial x - \partial u/\partial y$ and it is in the z direction. The positive and negative vorticity appear in pairs behind the blade. The vorticity behind the tip of the blade seems stronger than the ones behind other sections of the blade.

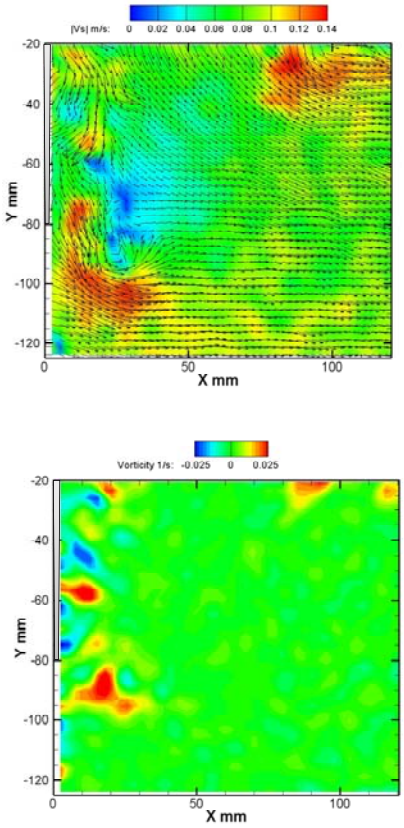

Fig. 25. a) Instantaneous subtracted velocity vector field and contour plot, b) Instantaneous vorticity ω immediately behind the turbine blade

To study the change of the wake behind the turbine with evolution in time, a series of instantaneous images were taken with time interval of 2 ms shown in Fig. 26. The first image in the sequence was captured when the blade was aligned with the laser sheet. The contour plots represent the non-dimentionalized x direction velocity u by the free stream velocity U_∞. As can be seen, the blade creates a low velocity spot immediately behind it which travels downstream with time. The x direction velocity u increases f outside the blades in the radial direction.

The tip of the blade creates a coupled high and low velocity region which indicates the occurrence of vortices. The vortex from the tip also travels downstream and become weaker in the mean time.

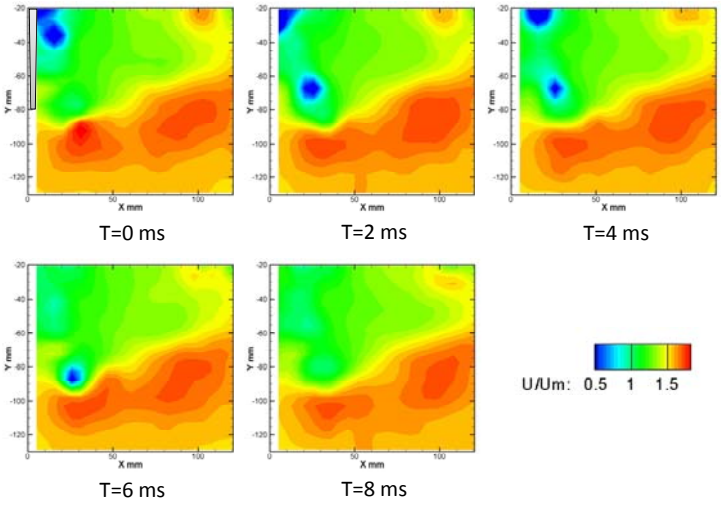

Fig. 26. Time evolution of non-dimentionalized x direction velocity behind the turbine wake

The time-resolved PIV experiment resolved the flow field of the turbine near wake with high temporal and spatial resolution. Further experiments will be done to study the downstream behavior of the wake and to reconstruct the quasi-instantaneous spatio-temporal representation under the assumption of Taylor's frozen hypothesis.

ACKNOWLEDGMENTS

We would like to thank C. Day and K. Guevarra for their help in the design of the rotor.

We would also like to thank Mr. J. Petrowski for creating the physical model.

REFERENCES

Burton, T., D. Sharpe, N. Jenkins, and E. Bossanyi. 2001. 'Wind Energy Handbook'. *Wind Engineering* 25, no. 3: 197–199.

Giguere, P., and M. S. Selig. 1999. Design of a tapered and twisted blade for the NREL combined experiment rotor. *NREL/SR*: 500–26173.

Glauert, H. 1935. Airplane propellers. *Aerodynamic theory* 4: 169–360.

Grant, I., M. Mo, X. Pan, P. Parkin, J. Powell, H. Reinecke, K. Shuang, F. Coton, and D. Lee. 2000. An experimental and numerical study of the vortex filaments in the wake of an operational, horizontal-axis, wind turbine. *Journal of Wind Engineering and Industrial Aerodynamics* 85, no. 2: 177–189.

Grant, I., and P. Parkin. 2000. A DPIV study of the trailing vortex elements from the blades of a horizontal axis wind turbine in yaw. *Experiments in Fluids* 28, no. 4: 368–376.

Haans, W., T. Sant, G. van Kuik, and G. van Bussel. 2005. Measurement of tip vortex paths in the wake of a HAWT under yawed flow conditions. *Journal of Solar Energy Engineering* 127: 456.

Hand, M. M., D. A. Simms, L. J. Fingersh, D. W. Jager, J. R. Cotrell, S. Schreck, and S. M. Larwood. 2001. *Unsteady aerodynamics experiment phase vi: Wind tunnel test configurations and available data campaigns*. NREL/TP-500-29955, National Renewable Energy Lab., Golden, CO.(US).

Hansen, M. O.L. 2008. *Aerodynamics of wind turbines*. Earthscan/James & James.

Hirahara, H., M. Z Hossain, M. Kawahashi, and Y. Nonomura. 2005. Testing basic performance of a very small wind turbine designed for multi-purposes. *Renewable energy* 30, no. 8: 1279–1297.

Hossain, M. Z., H. Hirahara, Y. Nonomura, and M. Kawahashi. 2007. The wake structure in a 2D grid installation of the horizontal axis micro wind turbines. *Renewable Energy* 32, no. 13: 2247–2267.

Massouh, F., and I. Dobrev. 2007. Exploration of the vortex wake behind of wind turbine rotor. In *Journal of Physics: Conference Series*, 75:9.

Medici, D., and P. H. Alfredsson. 2006. Measurements on a wind turbine wake: 3D effects and bluff body vortex shedding. *Wind Energy* 9, no. 3 (5): 219-236. doi:10.1002/we.156.

Myers, L., and A. S. Bahaj. 2006. Power output performance characteristics of a horizontal axis marine current turbine. *Renewable energy* 31, no. 2: 197–208.

Prandtl, L., and A. Betz. 1927. *Vier abhandlungen zur hydrodynamik und aerodynamik*. Selbstverlag des Kaiser Wilhelm-Instituts für Strömungsforschung.

Tangler, J., and J. D Kocurek. 2005. Wind turbine post-stall airfoil performance characteristics guidelines for blade-element momentum methods. In *43rd AIAA Aerospace Sciences Meeting and Exhibit*.

Tangler, J. L. 2002. Nebulous Art of Using Wind-Tunnel Airfoil Data for Predicting Rotor Performance: Preprint. In *Presented at the 21st ASME Wind Energy Conference, Reno, NV (US), 01/14/2002–01/17/2002*.

Vermeer, L. J., J. N. Sorensen, and A. Crespo. 2003. Wind turbine wake aerodynamics. *Progress in aerospace sciences* 39, no. 6-7: 467–510.

Viterna, L. A., and R. D. Corrigan. 1982. Fixed pitch rotor performance of large horizontal axis wind turbines.

Whale, J., C. G. Anderson, R. Bareiss, and S. Wagner. 2000. An experimental and numerical study of the vortex structure in the wake of a wind turbine. *Journal of Wind Engineering & Industrial Aerodynamics* 84, no. 1: 1–21.

ANNEX A

BLADES GEOMETRIES

Here, it is shown a schematic view of the blade from NREL (Fig. 27). Table 1 shows numerical values for each station for NREL blade (a)) and the new model blade (b)).

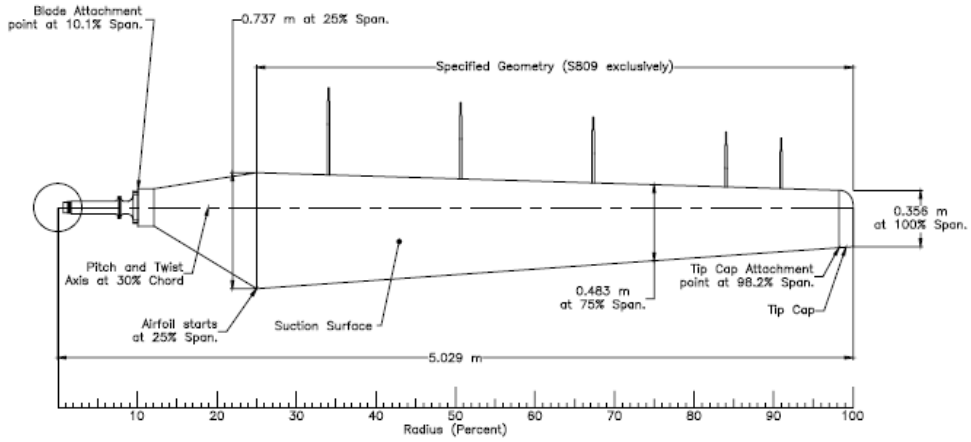

Fig. 27. Rotor blade dimensions (Hand et al. 2001)

Radial station (m)	Chord (m)	Twist (deg)
HUB		
1.0085	0.349	TRANS
1.0675	0.441	TRANS
1.1335	0.544	TRANS
1.2580	0.737	20.050
1.3430	0.728	18.074
1.5100	0.711	14.292
1.5220	0.710	14.040
1.6480	0.697	11.909
1.7980	0.682	9.670
1.9520	0.666	7.979
2.0750	0.654	6.750
2.3520	0.626	4.840
2.6280	0.598	3.480
2.9050	0.570	2.400
3.1810	0.542	1.510
3.4580	0.514	0.760
3.7350	0.486	0.090
3.7720	0.483	0.000
4.0110	0.459	-0.550
4.2880	0.431	-1.110
4.6960	0.389	-1.352
4.7800	0.381	-1.469
5.0000	0.358	-1.775
5.0300	0.356	-2.000

Radial station (m)	Chord (m)	Twist (deg)
HUB		
0.026258	0.008668	TRANS
0.035129	0.007276	TRANS
0.040099	0.013877	TRANS
0.042445	0.017535	TRANS
0.045070	0.021630	TRANS
0.050020	0.029304	TRANS
0.053400	0.028946	27.875917
0.060040	0.028270	25.453494
0.060517	0.028231	25.279842
0.065527	0.027714	23.533078
0.071491	0.027117	21.550862
0.077614	0.026481	19.652154
0.082505	0.026004	18.220231
0.093519	0.024891	15.309678
0.104493	0.023777	12.795491
0.115507	0.022664	10.611868
0.126481	0.021551	8.731961
0.137495	0.020437	7.098204
0.148509	0.019324	5.682766
0.149980	0.019205	5.499641
0.159483	0.018250	4.447862
0.170497	0.017137	3.379423
0.186720	0.015467	2.059449
0.190060	0.015149	1.811790
0.198807	0.014235	1.230905
0.200000	0.014155	1.100000

Table 1 R**ot**or blade stations characteristics a) NREL blade (Hand et al. 2001), b) New model blade

ANNEX B

AIRFOILS PROPERTIES

Here, it is shown a schematic view of the blade from NREL (Fig. 27). Table 1 shows numerical values for each station for NREL blade (a)) and the new model blade (b)).

α (deg)	C_l	C_d
-20.1	-0.55	0.2983
-18.2	-0.65	0.2955
-16.2	-0.80	0.1826
-14.1	-0.79	0.0793
-12.1	-0.70	0.0547
-10.2	-0.63	0.0401
-8.2	-0.58	0.0266
-6.2	-0.61	0.0183
-4.1	-0.40	0.0004
-2.1	-0.16	0.0009
0.0	0.07	0.0022
2.1	0.30	0.0037
4.1	0.55	0.0050
6.1	0.79	0.0063
8.2	0.90	0.0096
10.1	0.94	0.0231
11.2	0.93	0.0236
12.2	0.97	0.0368
13.3	1.00	0.0551
14.2	1.02	0.0618
15.2	1.03	0.0705
16.2	1.01	0.0880
17.2	0.95	0.1043
18.1	0.90	0.1325
19.2	0.78	0.3474
20.0	0.67	0.3211
22.1	0.70	0.3699
24.0	0.77	0.4348
26.1	0.91	0.5356

α (deg)	C_l	C_d
0.0	1.231	0.06467
0.5	1.282	0.06245
1.0	1.336	0.06407
1.5	1.390	0.06598
2.0	1.443	0.06751
2.5	1.493	0.07038
3.0	1.939	0.00983
3.5	1.600	0.07565
4.0	1.653	0.07731
4.5	1.698	0.07512
5.0	1.750	0.07700
5.5	1.798	0.08046
6.0	1.850	0.08188
6.5	1.898	0.08518
7.0	1.950	0.08613
7.5	1.997	0.09023
8.0	2.048	0.09602
8.5	2.093	0.09712
9.0	2.140	0.09973
9.5	2.190	0.10466
10.0	2.229	0.10905
10.5	2.458	0.09979
11.0	2.496	0.10585
11.5	2.533	0.11162
12.0	2.565	0.11455
12.5	2.600	0.11991
13.0	2.638	0.12238
13.5	2.676	0.12694
14.0	2.712	0.13346
14.5	2.742	0.13608
15.0	2.769	0.14025

Table 2 Wind tunnel profile coefficient a) S809 airfoil (Hand et al. 2001), b) GOE 531 airfoil